

# Particle In-Flight Velocity and Dispersion Measurements at Increasing Particle Feed Rates in Cold Spray

M. Meyer<sup>1</sup> · S. Yin<sup>1</sup> · R. Lupoi<sup>1</sup>

Submitted: 27 May 2016/in revised form: 13 October 2016/Published online: 8 December 2016  
© ASM International 2016

**Abstract** Cold spray (CS) is attracting interest of research and industry due to its rapid, solid-state particle deposition process and respective advantages over conventional deposition technologies. The acceleration of the particles is critical to the efficiency of CS, and previous investigations rarely consider the particle feed rate. However, because higher particle loadings are typically used in the process, the effect of this cannot be assumed negligible. This study therefore investigates the particle velocities in the supersonic jet of an advanced CS system at low- and high pressure levels and varying particle feed rates using particle image velocimetry. The particle dispersion and velocity evolution along the jet axis were investigated for several feedstock materials. It was found that the average particle velocity noticeably decreases with increasing particulate loading in all cases. The velocity distribution and particle dispersion were also observed to be influenced by the feed rate. Effects are driven by both mass loading and volume fraction, depending on the feedstock's particle velocity parameter. Increased particle feed rates hence affect the magnitude and distribution of impact velocity and consequently the efficiency of CS. In particular, numerical

models neglecting this interconnection are required to be further improved, based on these experimental studies.

**Keywords** cold spray · particle feed rate · particle image velocimetry · particle velocity · phase coupling

## Introduction

Cold spray (CS) is a coating manufacturing process, in which a feedstock powder is deposited onto a substrate by means of high-velocity impacts and solid-state deformation. As the process makes use of the high kinetic energy of the particles obtained from a supersonic process gas rather than their thermal energy, it allows for very low temperature levels compared to other coating technologies. It eliminates or minimizes the disadvantages of melting, and hence, it provides a possibility to coat oxidization-sensitive materials and material combinations with different melting temperatures (Ref 1, 2). It is generally accepted that for deposition to occur a critical impact velocity must be crossed. This represents a threshold value that makes the particle acceleration a critical aspect of the technology (Ref 3, 4). Each material combination is characterized by a specific critical speed level. Both experimental and numerical studies on the two-phase nozzle flow were conducted in the past decades, yielding to the main parameters for gas and particulate acceleration. Primarily, the gas stagnation pressure and temperature (Ref 5, 6), the gas species (Ref 7, 8) and the powder injection conditions (Ref 9, 10) are important. Another critical parameter is the particle material and size, as the larger and heavier particles are the less susceptible to the flow, having a much higher characteristic reaction time (Ref 11–13), whereas the particle shape is connected to the drag coefficient (Ref

---

This article is an invited paper selected from presentations at the 2016 International Thermal Spray Conference, held May 10–12, 2016, in Shanghai, P.R. China, and has been expanded from the original presentation.

---

✉ M. Meyer  
meyerm@tcd.ie

R. Lupoi  
lupoir@tcd.ie

<sup>1</sup> Department of Mechanical and Manufacturing Engineering, Trinity College Dublin, The University of Dublin, Parsons Building, Dublin 2, Ireland

14, 15). With the objective of analyzing the gas and particle dynamics, different optical measurement techniques were employed in CS. Schlieren photography was frequently used to visualize the flow features. Only resolving the density gradients of the gas phase, however, impedes quantification of the velocity and particle motion. Therefore, non-intrusive velocity measurement techniques were used, firstly by Gilmore et al. (Ref 16) who recorded the particle velocity by a laser-two-focus (L2F) apparatus and, inter alia, could observe a particle feed rate link to exit velocity. Due to the low spatial resolution and precision of L2F, many researchers subsequently concentrated on doppler picture velocimetry (DVP), which is described in detail in (Ref 17) and is used for rather small particle densities, such that the particle loading effect was not of interest. Particle image velocimetry (PIV) or similar techniques, such as tracking techniques, could be used to record instantaneous particle velocity distributions throughout the field of measurement without any scanning procedure. In this concern, several researchers facilitated results based on a single-frame triple-pulse particle tracking technique (Ref 18–20). In particular, Pardhasaradhi et al. (Ref 21) used this approach to measure the particle exit speed of different nozzles under varying conditions. It was found that the effect of the particle loading had a negligible countereffect on the particle dynamics within the scope of measurement, attributed to a low-mass fraction of the discrete phase. Nevertheless, depending on the particle feed rate and the relative gas consumption, the discrete phase loading can increasingly affect the acceleration process at higher feed rate levels. Results demonstrated by Samareh et al. (Ref 22) indicated that the gas flow structures change and the particle speed reduces as their mass fraction increases. Accordingly, a study by Lupoi (Ref 23) showed that a number of experimental observations with various nozzle geometries could not be explained by one-way coupling CFD techniques. An improvement in the computations was shown to be achievable when increasing the detail of phase coupling for such experiments by Meyer and Lupoi (Ref 24). As for higher particle feed rates, a work by Pattison et al. (Ref 25) showed an experimental optimization involving a full 2D-velocity field deduction using PIV in its usual sense. Similarly, Zahiri et al. (Ref 26) demonstrated particulate plume characteristics in CS with PIV. Although a sufficiently high particle density must be implied to enable the field measurements with PIV in these studies, as no usage of ensemble of correlation algorithms is reported, the studies did not consult the links of particle loading to velocity results. There is no doubt that faster processing times in CS manufacturing applications can be achieved by higher feed rates. A cost analysis of the CS process by Stier (Ref 27) provides evidence that it is important to understand the mass loading effect also on an economical level,

as it enables the optimization of gas and powder consumption without loss of deposition efficiency. In order to start understanding the detailed effect of the particle feed rate as a process parameter, this work aims to investigate the particle velocity in the jet of a cold spray system working under low pressure and high pressure conditions in dependence of the particle feed rate using PIV, in combination with a tracking algorithm for the identification of single particle vectors. Feedstock materials are varied and measured under different flow conditions aiming to identify driving mechanisms of the phase interactions.

## Methods

### Cold Spray System and Materials

Figure 1(a) illustrates a schematic of the experimental arrangement, including PIV and the CS process. The nitrogen gas flow was provided by a supplier, delivering the settings of 30 and 15 bar constant pressure at the nozzle inlet. The gas line was split into two lines, a main line,

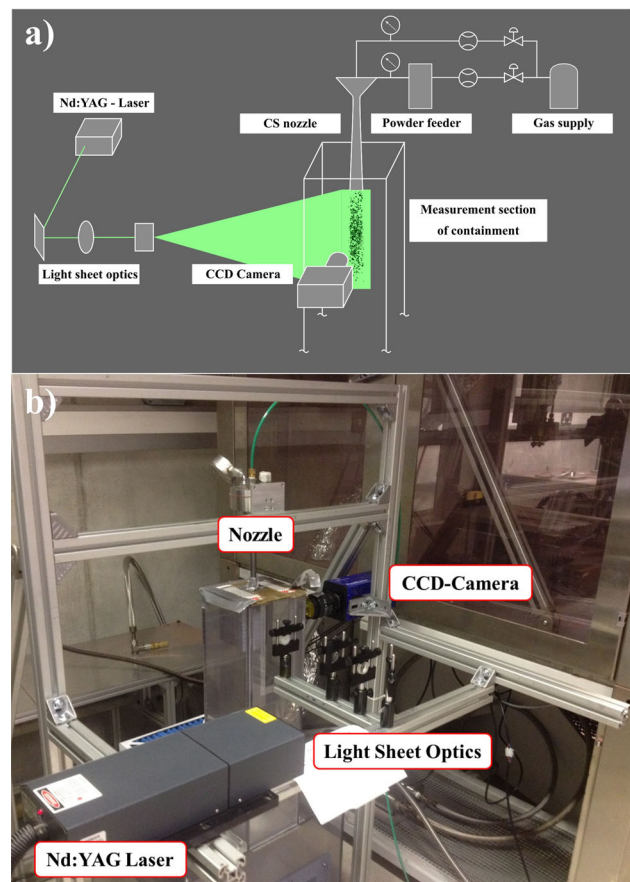


**Fig. 1** (a) Scheme of experimental setup and (b) picture of the measurement system in the laboratory

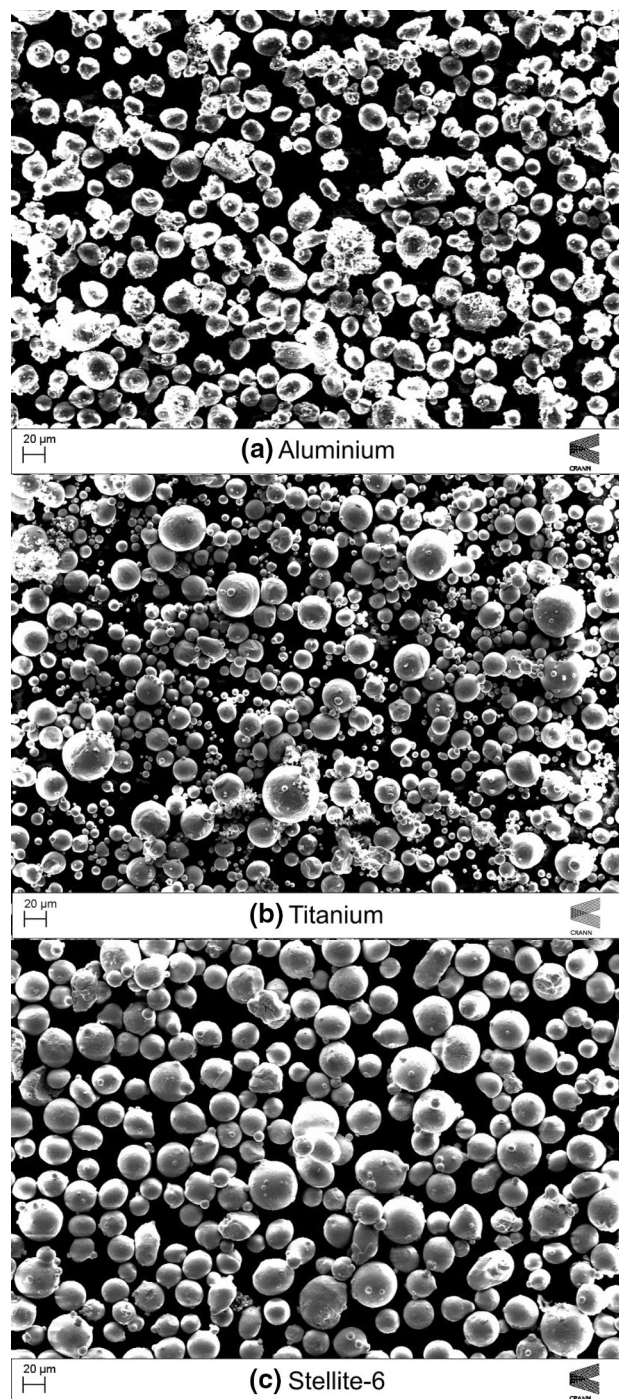
which was connected to the nozzle head, and the powder feeder line; both of which comprised flow meters and pressure gauges. The wheel type powder feeder included a load cell to measure the mass feed rate of powder. The setting of powder feed rate was increased according to the capabilities of the feeder for each material. Downstream, the gas-solid mixture then merged with the main flow in the nozzle head. The in-house nozzle design of de-Laval converging/diverging shape had a full length of 210 mm, a 2-mm throat diameter and a 6-mm exit diameter. The velocity measurement area was oriented within the longitudinal direction and with a length of 50 mm from the nozzle exit, such that the relevant region of the particle jet was covered. The nozzle sprayed into the measurement section of an enclosed area, which ensured undisturbed flow in absence of a substrate. Figure 1(b) shows the CS-PIV setup in TCD.

Figure 2 shows scanning electron microscope (SEM) images, created with a Zeiss Ultra Plus scanning electron microscope, of the three different materials used in this study. Commercially pure aluminum and titanium (CP2) were used as a rather light-weight and an intermediately heavy material. In addition, stellite-6, a cobalt-chrome alloy which is highly relevant for CS applications with well-known corrosion resistance characteristics, was compared as a higher density feedstock. Table 1 summarizes the material properties and testing conditions. It was not possible to obtain useful results for titanium at 30 bar pressure; frequently, particles started glowing due to collisions with the nozzle wall close to the exit, which interfered with the imaging technique.

Figure 3 presents the size distributions of the three used powders in terms of their incremental and cumulative volume frequency obtained by a Sympatec HELOS laser diffraction particle size analyzer. Each measurement was carried out in quadruplicate on three different samples of each powder. The powder was dispersed in water using a magnetic stirrer rotating at 1200 RPM in tandem with an ultrasonic probe. The size ranges and distributions are very similar for all three powders with particles between 10 and 60  $\mu\text{m}$ . Stellite-6 exhibits a slightly narrower distribution, and titanium comprises some more small particles toward the low end of the range. The volume mean diameter (VMD) is approximately 30  $\mu\text{m}$  for all feedstock materials. It is interesting to note that this implies a correspondence of the particle velocity parameters ( $\text{PVP} = d_p \rho_p$ ) to the material density only. PVP was analytically shown to be inversely proportional to the particle acceleration (Ref 28).

### Measurement Set-Up

Particle image velocimetry was used to optically measure the particle velocity within the jet. They were illuminated



**Fig. 2** Comparison of SEM images of measured CS powders: (a) aluminum, (b) titanium, (c) stellite-6

with two subsequent laser pulses formed to a light sheet in the plane of measurement. A camera system captured two images of the scattered light, respectively, with varying pulse separation time depending on the conditions. These images were processed by a cross-correlation algorithm, deducing the particle displacement, which corresponds to velocity information by knowledge of the pulse separation.

**Table 1** Powder materials and spray conditions

Feedstock	Stellite-6 (ST)	Titanium (TI)	Aluminum (AL)
Density (kg/m <sup>-3</sup> )	8440	4500	2700
Pressure (bar-g)	30/15	15	30/15
Temperature (K)	290	290	290

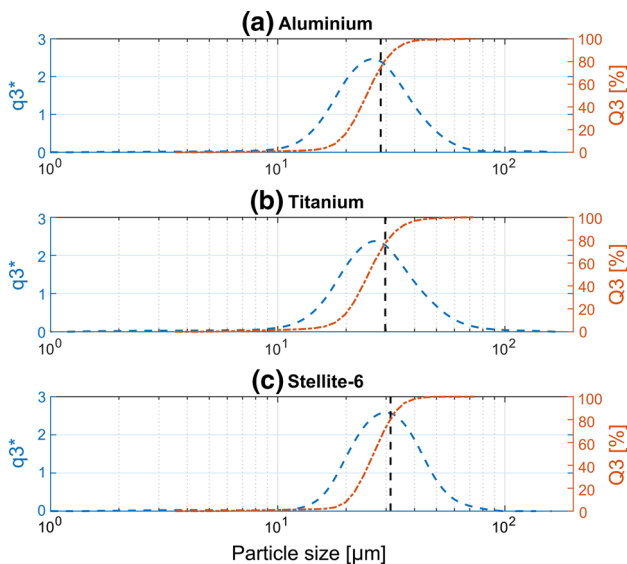


**Fig. 3** Particle size distribution for (a) aluminum (b) titanium (c) stellite-6

As the feedstock particles are measured directly in CS, the gas phase was not subject to measurement in this study. The particle Stokes number  $St = \tau_p/\tau_f$ , expressed as the ratio of the particle reaction time and a characteristic fluid time, can be in the order of unity or higher, which means that due to significant lag between particle and fluid motion, no information about the fluid can be inferred. A Nd:YAG Laser with a wavelength of 532 nm and 6-ns pulse duration was used as the light source at 4-Hz repetition rate. The maximal displacement of particles during a single pulse was, hence, in the order of 0.07 px. The pulse separation time was adjusted between 1 and 2 μs depending on the velocity level aiming for an approximate displacement of particles of 10 px allowing for a prolonged dynamic range toward the lower end. The light sheet was formed by a telescope of spherical lenses for the sheet thickness of approximately 1 mm and a cylindrical lens for the sheet width of 60 mm, respectively, illuminating the plane of symmetry downstream of the nozzle. A monochromic camera with a resolution of 1280 × 1024 pixels of 6.7-μm pixel size and a 12-bit dynamic range delivered the consecutive image pairs. The camera lens aperture was set to f/8.0 in order to minimize lens aberrations. The imaging magnification of 0.15666 lead to theoretical minimum particle image sizes due to diffraction between 1.8 and

2.3 px, whereas the actual observed values were found between 2 and 4 px. The depth of field was approximately 9 mm accordingly. The repetition rate was limited by the CCD readout time of the camera, such that the entire evolution of the particles through the flow field could not be tracked considering the high order of the present velocities. The preprocessing of images included a standard background subtraction of an averaged image from 100 samples in the absence of particles and high-pass filtering of the raw data to reduce stationary image features and low-frequency background variations. The high-pass filter was applied in form of a subtracted sliding average with a kernel size of 5 px, which fulfills the requirement to be larger than the particle images. The image processing involved a two-step approach, in which a double-frame cross-correlation is used for a coarse velocity field as an estimator and an additional particle tracking velocimetry (PTV) algorithm is used to identify the single particle vectors. Along with the hardware, the algorithms were produced by *LaVision* as part of *DaVis v7.2*. The cross-correlation algorithm was a multi-pass with reducing interrogation window size from 32 × 32 px to 16 × 16 px with 50% window overlap. Computation of the spatial correlation was performed by a cyclic FFT, and the peak-fitting algorithm was the standard three-point Gaussian fit, followed by a median filter for removal of outliers. The subsequent detection of single particles was performed with a gray-value threshold of the images. By applying the correlation algorithm on 16 × 16 px interrogation windows that were centered on each first exposure particle image and pre-shifted by the field predictor, the displacement was found by evaluating the existence of a particle image in the second exposure.

The measurement error in PIV and PTV has a multitude of sources, of which the most important are optical uncertainties (e.g., lens aberrations and calibration errors) and algorithm-related errors, consisting of an rms displacement error and a bias or “peak-locking” error. Deducing the uncertainty in calibration from the target plane images, we estimate a maximal calibration uncertainty of 0.03 px for a 10 px displacement. Based on the peak ratio of the primary and secondary peak in the correlation plane, the rms error could be estimated in the order of 1.3%. Conservatively, we corrected this value according to the uncertainty introduced by the PTV stage of the algorithm and the reduced correlation window size based on previous thorough analysis of the algorithm (Ref 29), which results in an rms error of 0.18 px or 1.8% on the average displacement. Lastly, the used algorithm for particle tracking was shown to have exceptionally low bias error, even for particle image sizes <2 px (Ref 29). Because the particle image size was noticeably larger, reducing the potential for a bias error, this source was not

considered further. In addition, repeatability was assured and the respective standard deviation as well as the deduced PIV errors were included in the reported errors bars of the measurements given in sections to follow.

## Results and Discussion

### Flow and Loading Conditions

As wheel speed of the powder feeder was increased, the mass feed rate of particles depends on the powder in use and the spray conditions. This results in varying ranges of feed rates for the different materials. For aluminum, having the lowest density, it was possible to increase the mass feed rate to just below 150 g/min (corresponding to full wheel speed), whereas titanium could be fed at a maximum of 350 g/min. For stellite-6 even higher feed rates would have been possible, which would be beyond the scope of interest of this study. Figure 4 shows the connection between the particle feed rate and the corresponding relative mass loading  $Z$  as the ratio of the overall particle and gas mass flow rate in the nozzle. The gas flow conditions were measured to be constant for all measurements of each pressure setting, yielding 0.0136 kg/s at 15 bar and 0.0271 kg/s at 30 bar inlet pressure. Due to this, one can see the linear connection to the relative loading. The gas flow approximately doubles when increasing the pressure from 15 to 30 bar, which results in a steeper slope for the low pressure setting. One can hence expect any loading effect to be more drastic for such case;  $Z$  goes up to a maximum of 0.4, but even at lower values, the mass fraction is high enough for the phase interaction to become significant.

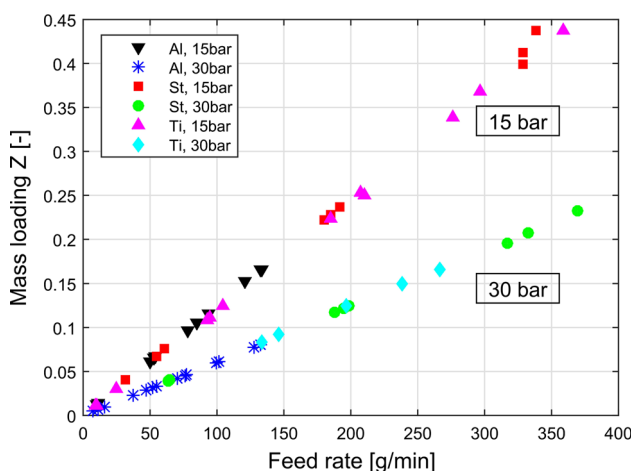


**Fig. 4** Verification of linear correlation between particle feed rate and relative mass loading

One of the concerns that typically arise from optical speed measurements in cold spray is the uncertainty related to the varying particle sizes. This does not represent a measurement error per se, but it can limit the representative character of the findings. In this context, it should be distinguished between the measurement uncertainty discussed previously and this phenomenon of a bias of correctly identified particle velocity vectors toward a specific size range. The measurement principle takes advantage of the Mie scattering of coherent light, which is strongly dependent on the particle size. In an idealized scenario, only a single particle size should be present, for the light to be scattered and diffracted in the same way for all particles. This is optimal for the correlation peak quality when processing the images on the one hand, and for the capturing of all particles present in the flow on the other. In other words, when measuring a wider size distribution of particles, not only the correlation becomes more difficult, also the measurement setup cannot be adjusted for all sizes, resulting in a bias of the velocity measurement to a specific preferred size. For example, small particles are not illuminated strongly enough and are kept from being measured. One way to assess this and make an attempt in quantifying the uncertainty is given by a comparison of the “normalized” dynamic range of the measured velocities to the dynamic range of sizes. More precisely, based on simple analytic equations, the approximated proportionality  $v_p \propto \sqrt{1/d_p}$  between particle velocity and diameter can be shown (Ref 30), such that this quantity is used for the comparison. Figure 5 depicts the respective histogram for the velocity range and the  $\sqrt{1/d_p}$ -range for titanium as an example. It shows that the higher end of the velocity diminishes faster than the size range, which means that the

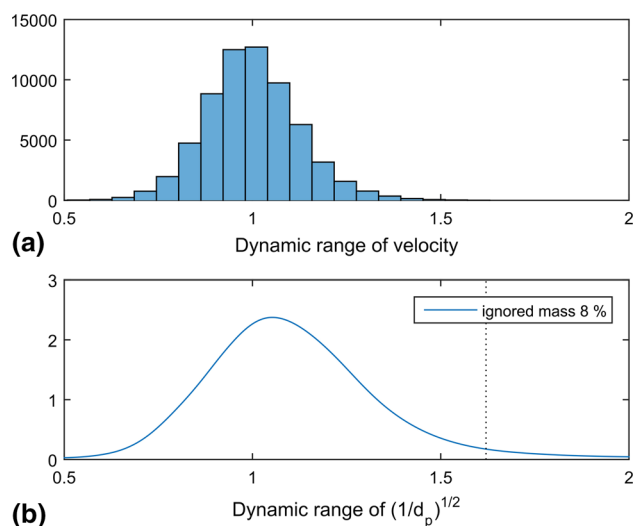


**Fig. 5** Comparison of the normalized dynamic ranges of velocity (a) and particle size (b)

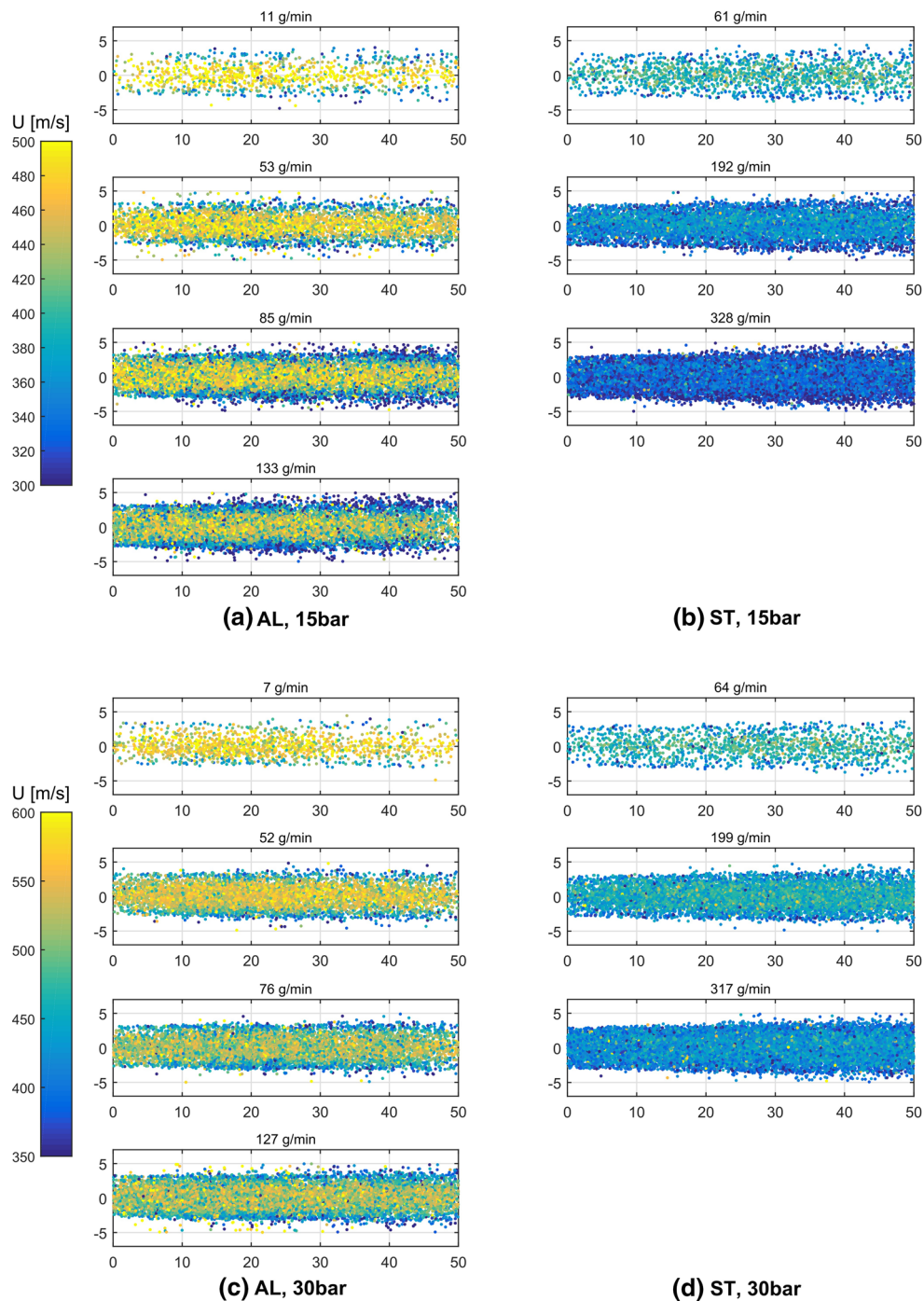
small end of particle sizes is ignored to some extent. Calculating the capped portion of particles, it must be estimated that about 8% of the particle mass may be excluded from the measurement. For stellite-6 and aluminum, these values were lower at 4 and 6%. Within this study, the small bias was accepted as it relates to the very small particles which also carry the highest risk of non-deposition due to deceleration in the bow shock in front of the substrate. However, for future studies, it is strongly recommended to use powders with very narrow size distribution for this type of technique.

### Velocity Distribution and Footprint

In order to compare the phase-coupling effect for the chosen set of materials, one can start by investigation of the particle velocity distribution under varying conditions. Figure 6 shows a comparison of the particle distributions in the plane of measurement. On the  $x$ -axis the streamwise direction is displayed from the nozzle exit down to a distance of 50 mm. On the  $y$ -axis the radial coordinate can be found. The subfigures represent increasing loading cases for aluminum and stellite-6 at 15 bar (a,b) and at 30 bar (c,d) pressure levels, respectively. The positions of detected particles are projected in the plane of measurement and colored by their velocity magnitude. In this test, no substrate was present. At the nozzle exit, each plot shows a narrow stream in the range of  $\pm 3$  mm (nozzle exit radius) of exiting particles that widens downstream until the plume approximately occupies the region from  $-5$  to 5 mm. This downstream dispersion results from the interaction of particles with turbulence, the shock waves forming in the gas jet and the shear layer at its edge. It can be seen that it is stronger for high loading cases, because a larger amount of particles experiences sideways forces and is pushed out of the jet core. Aluminum is more prone to this effect than the other materials; it exhibits a stronger dispersion away from the nozzle exit and it also shows a more noticeable deceleration of all particles with distance from the exit. Providing the lighter particles, it can be explained that the disintegrating gas jet dispenses its potential to accelerate the particles, which in turn aggravate the declining kinetic energy of the gas jet at higher loadings. Therefore, a higher overall decrease in velocity (of both the higher velocities in the jet core and the lower velocities at the boundaries) can be seen with growing feed rate. The higher the loading of particles is, the stronger the downstream deceleration becomes. For both materials, one can record that the dispersion is weaker for higher pressure. Consequently, the more momentum the particles have, the less susceptible they are to unfavorable deviations. At the lower pressure level, the gas nozzle flow is significantly over-expanded leading to stronger shock systems, which causes additional disturbance of the particle dynamics.

The observed aspects result in different particle velocity characteristics when changing materials and feed rates. As a result, the impact velocity footprint upon a substrate differs in its size and velocity range as well. It is, hence, interesting to investigate the particle velocity profiles at stand-off locations where a substrate could be placed. When choosing larger possible stand-off distances, indicators of the expected trends are more noticeable. Figure 7 therefore displays particle velocity profiles in the radial direction of particles which are located between 40 and 50 mm downstream from the nozzle exit, hence, on the far right side of the plots in Figure 6. In this illustration, each subplot shows data points for individual particle speeds and the curves are Gaussian fits. It should be noted that these fits are supposed to guide the eye for ease of comparison and explicitly not suggest as a physical trend, as there is no strict reason for the particle profiles to follow a normal distribution this close to the nozzle exit. However, as the underlying gas jet may approach a self-similar solution, a near-Gaussian gas velocity distribution plays a role in the driving mechanisms of the particle behavior, such that it is considered as an adequate fitting function. When opposing the different materials, a weaker curvature of the profiles can be noticed when going from aluminum through titanium to stellite-6. The maximum velocities of the profiles are located around the centerline, and the radial velocity drop associated with the curvature easily reaches 200 m/s for the light material, while for the alloy, it is only in the order of 50–70 m/s. This observation underlines that the light material is affected more than twice as much by the spreading of the gas jet. Note that this may result in lower deposition efficiency for lighter materials. At higher pressure, the curvature is slightly higher than for smaller pressure due to higher core gas velocity, and a shift of the maximum by about 23% for aluminum and 21% for stellite-6 can be registered. This is approximately the amount by which the velocities reduce when finally comparing the low-feed to high-feed cases. In this case, the slowest particles in the dilute cases are as fast as the fastest in the dense flow case. This reduction in maximal velocity is stronger for titanium and stellite-6, where the velocity profile flattens strongly. That is, relatively fast particles tend to occupy the areas further away from the centerline, resulting in a smaller velocity range due to profile curvature. This means that particles close to the center exhibit lower velocities at high loadings because the gas core is weaker, while particles that are pushed outwards retain a higher portion of their speed because of their inertia. For aluminum, the curvature changes only little, which is plausible due to faster deceleration when entering regions of negative relative gas-particle velocity. In every case, the low-feed results show particles mainly within the region of the nozzle exit diameter ( $\pm r_{\text{exit}}$ ), whereas the high feed

**Fig. 6** Scatter of single particle velocities in the x-y-measurement plane using the PIV (0 = nozzle exit). Comparison of aluminum and stellite-6 velocity distribution and particle dispersion for increasing pressure and mass loading



indicates a significantly stronger dispersion in the realm of  $\pm 4$  to  $\pm 5$  mm, which quantitatively supports earlier findings (Ref 31).

These observations are important considering effective deposition of different materials at increasing particle feed rates. The pressure level, the feed rate and the radial profiles affect the velocity of particles and hence the impact conditions. It is important to note that due to the absence of a substrate, the additional effects of the bow shock system upon impact are not analyzed. However, the analyzed

velocity reductions can lead to subcritical impact velocities after passing through the shock and hence significantly reduce deposition efficiency.

### Mean Velocity Change and Phase Interaction Drivers

As the experiments were conducted repeatedly and provided spatially resolved data, more insight can be gained analyzing the overall effect by means of the average

**Fig. 7** Radial velocity profiles at 40–50mm distance from nozzle exit by the PIV apparatus. Data points represent single particle velocities, lines indicate profile trend as Gaussian fits

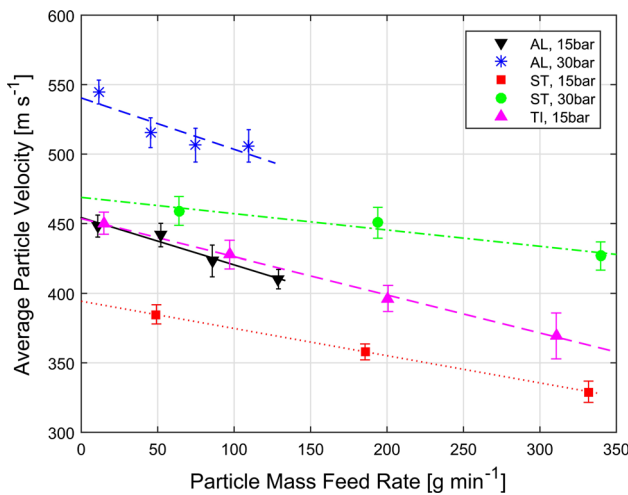
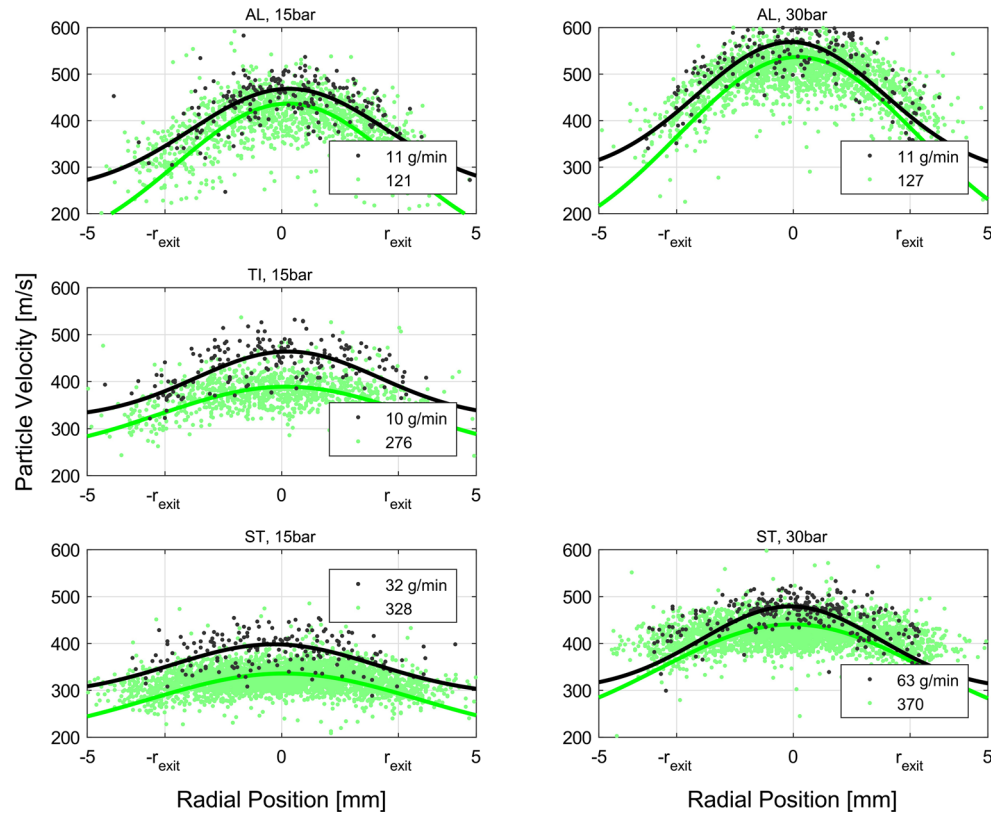


**Fig. 8** Comparison of material behavior due to increasing particle feed rate using spatial and temporal average of particle velocity at the nozzle exit

change in particle velocity. This averaging was conducted over all measured particles, hence, including changes with position, and over all image sets, as a temporal average. Figure 8 summarizes the respective results. The line segments are least-square linear fitting curves for the data points, clarifying the change in velocity. The error bars comprise  $2\sigma$ -confidence intervals and the inherent uncertainty associated with the optical analysis.

With focus on the low pressure velocity values at very low-feed rates, it can be seen that due to the different material densities, the velocity levels differ. Stellite-6 exhibits the lowest velocity, ca. 55 m/s lower than aluminum. As the pressure level is increased, this low-feed velocity increases by about 20% for both stellite-6 and aluminum, or by 75 and 90 m/s, respectively. Most importantly, one can clearly see a decrease in average velocity for all materials at given conditions. This trend appears to be approximately linear in the given range of feed rates and slightly less severe at higher pressure. It is essential to note that the loss in particle velocity is different from case to case, as it can be as high as 10% for aluminum, and up to 16 and 20% for stellite-6 and titanium, respectively, when taking into account the extended range of particle feed rates explored. Interestingly, this implies that the same amount of additional particle mass injected in the nozzle does not induce the same velocity loss. More precisely, the slope for stellite-6 is less steep than for titanium, and the reaction of aluminum is the most severe. According to the observation, the effect becomes more significant with decreasing density. Based on the conservation of momentum and energy, it can be argued that the velocity of the discrete phase must drop because its mass increased by a specific amount. However, for the different materials, the given mass feed rate corresponds to different numbers of particles and volumetric feed rates, and



therefore to different volume fractions. For example, 100g/min feed rate corresponds to volume feed rates of 0.0118 and 0.037 L/min for stellite-6 and aluminum, respectively. Moreover, the gas consumption and the resulting mass and volume flux of gas are not constant. If the effects are more complex, the additional influence on the average particle dynamics with a change in volume fraction and relative mass loading must be investigated.

In this regard, the quantities were non-dimensionalised in the following way. The velocity is normalized by the very low-feed limit of each case, denoted  $v_{p0}$ , that can be interpreted as the particle velocity obtainable without any feeding effect. The feed rate and the measured gas flux were used to calculate firstly the relative mass loading  $Z$ , and secondly the volume fraction of particles  $F$  with respect to gas conditions in the nozzle throat. Figure 9 presents the scaled data along with a few interesting novel insights. The top subfigure (a) shows that stellite-6 is the least susceptible pertaining to a change in relative mass loading, titanium is intermediate and aluminum reacts the most severely. The lighter the material, the stronger the reaction, which suggests that the particle volume plays a role, since the same increase in aluminum mass

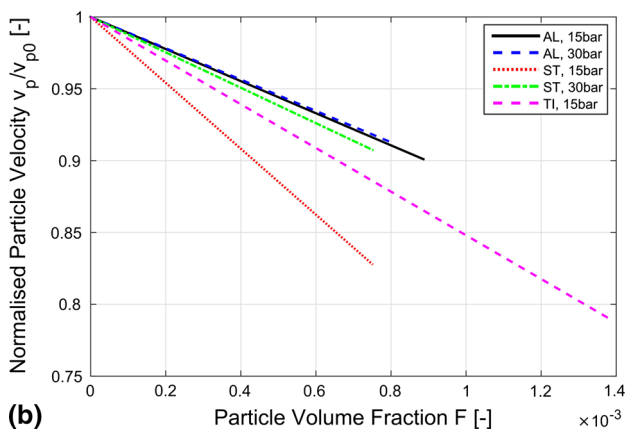
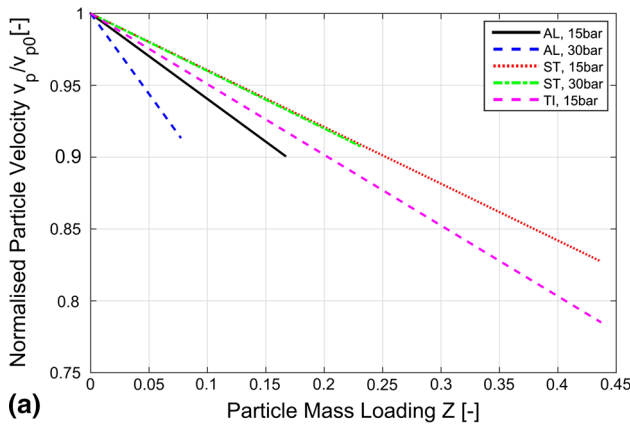


**Fig. 9** Normalized velocity over relative mass loading (a) and particle volume fraction (b)

corresponds to a much higher volumetric increase than in case of stellite-6. Moreover, the pressure increase seems to have an aggravating effect on the light and almost no effect on the heavier material. The bottom figure (b) shows changes due to volume fraction accordingly. Here, aluminum reacts the weakest and almost independently from pressure and stellite-6 shows the strongest susceptibility.

Figure 10 isolates these findings by showing the magnitudes of gradients pertaining to mass (a) and volume fraction (b) over the respective particle velocity parameter. The gradients are used as indicators for the susceptibility of the respective characteristic particles to loading effects by these two different driving factors. In this article, the term “driving factor” refers to the quantity that represents the phase interaction mechanism and explicitly not to the quantity that has the most intense effect. The following analysis clarifies and defines these factors.

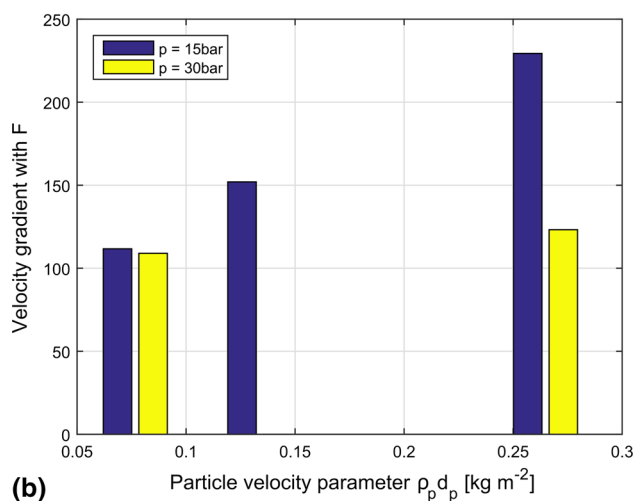
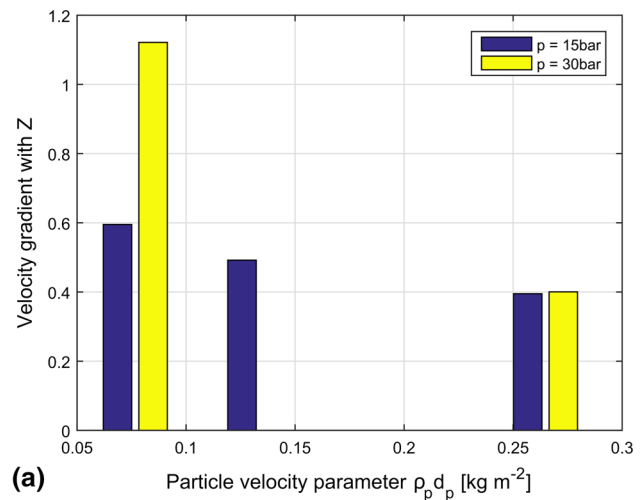


**Fig. 10** Gradient of velocity with mass loading (a) and with volume fraction (b) as a susceptibility indicator displayed over the particle velocity parameter

Focusing on (a), it is clear that the lower the PVP, the more prone the material is to mass fraction effects. This does not imply that mass fraction is the driving factor here. The contrary is the case, because at low PVP, the mass corresponds to a much higher volume than at high PVP. This is hence a volume-dependent interaction and it is aggravated strongly by pressure increase. If the underlying mechanisms are related to particle-particle interactions for instance, it is plausible, that respective losses are pressure-dependent. At high PVP, the pressure has almost no effect. This indicates that the character of the interaction mechanism is the same for both pressures. Hence, the mass loading can be identified as the driving mechanism for high-PVP materials. Physically, this can be interpreted as particle mass that needs to be accelerated by the mass flux of gas. Argued the other way around based on (b), the higher the PVP, the more prone the material becomes to volume-induced interaction effects, because the same volumetric increase corresponds to much higher mass increase—and mass becomes the more important driving mechanism for interaction. Increasing the pressure level now amends this situation and reduces the gradient for high PVP, because the lower the pressure, the smaller the gas mass flux and hence the more difficult the additional particle mass is accelerated. In turn, at low PVP almost no change with pressure is now registered, meaning that the mechanisms for both pressures are the same. This makes the volume fraction the driving factor for low PVP as indicated by the previous figure. For intermediate materials, both effects play an important role and the PVP is decisive for which the more dominant factor is; relative volume or relative mass.

Volumetric and mass effects can be linked, for instance, by particle-particle collisions, change in turbulence and dissipation, as well as locally very dense regimes (e.g., in the nozzle throat region). In order to quantify these effects, it would be necessary to investigate the particle behavior during acceleration, i.e., inside the nozzle. The importance of understanding these phase interaction mechanisms pertaining to the particle speed can be emphasized at the example of a steep deposition efficiency drop due to velocity decrease. Moreover, it is likely that also the particle temperature is affected by the loading with respective consequences on the window of deposition. However, it can neither be said at this point whether this is a significant influence nor can an experimental investigation be suggested. Common computational methods employing Eulerian-Lagrangian approach even with two-way coupled interaction are not able to mimic the findings from this study, because particle collisions and volumetric effects are inherently excluded. Improvement in the techniques used in CS simulations is therefore important to capture the character of phase interactions in detail.

## Conclusion

In cold spray, the acceleration of the particles is critical to efficiency, and previous fluid dynamic investigations rarely consider the particle feed rate important. However, higher particle loadings can change the process and induce noticeable effects on the particle dynamics. This study therefore experimentally investigated the particle velocities in the supersonic jet at lower and higher pressure level, analyzing the effect of varying particle feed rates on stellite-6, aluminum and titanium particles using PIV. The main novel findings are that the particle velocity decreases more strongly while traveling downstream at high loadings and that the radial velocity footprint becomes more flat in such case. Aluminum was found to be more prone to radial velocity decrease also for high-feed rates, but all materials show intensified particle dispersion at large distances from the nozzle exit. Moreover, the study found that the average particle velocity was reduced in every case when the particle loading was increased, in part as high as 20%. It was found that the materials behave differently when changing particle feed. The relative drop in velocity can be influenced by both the relative volume fraction and the relative mass loading. For limits of high particle velocity parameters the driving mechanism tends toward the mass loading, while at the limit of a low velocity parameter, the volume fraction is the more characteristic driver. It is proposed that complex processes which involve nonlinear effects play a role in this respect. Increased particle feed rates hence affect the magnitude and distribution of impact velocity and consequently the efficiency of cold spray. In particular, computational modeling approaches neglecting this interconnection are required to be further improved, based on experimental studies presented in this paper.

**Acknowledgments** The authors wish to acknowledge FP7 Marie Curie Actions (Grant 333663) for the financial support and to the CRANN Advanced Microscopy Laboratory (AML) for the cooperation, as well as to Dr. Tim Persoons (Trinity College Dublin) and Dr. Kevin McDonnell (University College Dublin) for the technical advice and support.

## References

1. A. Alkhimov, V.F. Kosarev, and A. Papyrin, Method of Cold Gas Dynamic Spraying, *Dokl. Acad. Nauk SSSR*, 1990, **315**(5), p 1062-1065
2. A. Papyrin, Cold Spray Technology, *Adv. Mater. Process.*, 2001, **159**(9), p 49-51
3. H. Assadi, F. Gärtner, T. Stoltenhoff, and H. Kreye, Bonding Mechanism in Cold Gas Spraying, *Acta Mater.*, 2003, **51**(15), p 4379-4394
4. M. Grujicic, C.L. Zhao, C. Tong, W.S. DeRosset, and D. Helfritch, Analysis of the Impact Velocity of Powder Particles in the Cold Gas Dynamic Spray Process, *Mater. Sci. Eng.*, 2004, **368**(1-2), p 222-230

5. T. Han, Z. Zhao, B.A. Gillispie, and J.R. Smith, Effects of Spray Conditions on Coating Formation by the Kinetic Spray Process, *J. Therm. Spray Technol.*, 2005, **14**(3), p 373-383
6. E.H. Kwon, S.H. Cho, J.W. Han, C.H. Lee, and H.J. Kim, Particle Behavior in Supersonic Flow During the Cold Spray Process, *Met. Mater. Int.*, 2005, **11**(5), p 377-381
7. T.C. Jen, L. Li, W. Cui, Q. Chen, and X. Zhang, Numerical Investigations on Cold Gas Dynamic Spray Process with Nano- and Microsize Particles, *Int. J. Heat Mass Transf.*, 2005, **48**(21-22), p 4384-4396
8. H. Katanoda, T. Matsuoka, and K. Matsuo, Experimental Study on Shock Wave Structures in Constant-Area Passage of Cold Spray Nozzle, *J. Therm. Sci.*, 2007, **16**(1), p 40-45
9. S. Yin, Q. Liu, H. Liao, and X.-F. Wang, Effect of Injection Pressure on Particle Acceleration, Dispersion and Deposition in Cold Spray, *Comput. Mater. Sci.*, 2014, **90**, p 7-15
10. S. Yin, X. Suo, H. Liao, Z. Guo, and X. Wang, Significant Influence of Carrier Gas Temperature During the Cold Spray Process, *Surf. Eng.*, 2014, **30**(6), p 443-451
11. F. Gärtner, T. Stoltenhoff, T. Schmidt, and H. Kreye, The Cold Spray Process and Its Potential for Industrial Applications, *J. Therm. Spray Technol.*, 2006, **15**(2), p 223-232
12. A. Sova, A. Okunkova, S. Grigoriev, and I. Smurov, Velocity of the Particles Accelerated by a Cold Spray Micronozzle: Experimental Measurements and Numerical Simulation, *J. Therm. Spray Technol.*, 2012, **22**(1), p 75-80
13. S. Li, B. Muddle, M. Jahedi, and J. Soria, A Numerical Investigation of the Cold Spray Process Using Underexpanded and Overexpanded Jets, *J. Therm. Spray Technol.*, 2011, **21**(1), p 108-120
14. X.-F. Wang, S. Yin, and B.P. Xu, Effect of Cold Spray Particle Conditions and Optimal Standoff Distance on Impact Velocity, *J. Dalian Univ. Technol.*, 2011, **51**(4), p 498-504
15. W.-Y. Li and C.-J. Li, Optimization of Spray Conditions in Cold Spraying Based on Numerical Analysis of Particle Velocity, *Trans. Nonferrous Met. Soc. China*, 2004, **14**(2), p 43-48
16. D.L. Gilmore, R.C. Dykhuizen, R.A. Neiser, T.J. Roemer, and M.F. Smith, Particle Velocity and Deposition Efficiency in the Cold Spray Process, *J. Therm. Spray Technol.*, 1999, **8**(4), p 576-582
17. H. Fukunuma, N. Ohno, B. Sun, and R. Huang, In-Flight Particle Velocity Measurements with DPV-2000 in Cold Spray, *Surf. Coat. Technol.*, 2006, **201**(5), p 1935-1941
18. B. Jodoin, F. Raletz, and M. Vardelle, Cold Spray Modeling and Validation Using an Optical Diagnostic Method, *Surf. Coat. Technol.*, 2006, **200**(14-15), p 4424-4432
19. F. Raletz, M. Vardelle, and G. Ezo'o, Critical Particle Velocity Under Cold Spray Conditions, *Surf. Coat. Technol.*, 2006, **201**(5), p 1942-1947
20. X.-J. Ning, Q.-S. Wang, Z. Ma, and H.-J. Kim, Numerical Study of In-flight Particle Parameters in Low-Pressure Cold Spray Process, *J. Therm. Spray Technol.*, 2010, **19**(6), p 1211-1217
21. S.P. Pardhasaradhi, V. Venkatachalapathy, S.V. Joshi, and S. Govindan, Optical Diagnostics Study of Gas Particle Transport Phenomena in Cold Gas Dynamic Spraying and Comparison with Model Predictions, *J. Therm. Spray Technol.*, 2008, **17**(4), p 551-563
22. B. Samareh, O. Stier, V. Lüthen, and A. Dolatabadi, Assessment of CFD Modeling via Flow Visualization in Cold Spray Process, *J. Therm. Spray Technol.*, 2009, **18**(5-6), p 934-943
23. R. Lupoi, Current Design and Performance of Cold Spray Nozzles: Experimental and Numerical Observations on Deposition Efficiency and Particle Velocity, *Surf. Eng.*, 2014, **30**(5), p 316-322
24. M. Meyer and R. Lupoi, An Analysis of the Particulate Flow in Cold Spray Nozzles, *Mech. Sci.*, 2015, **6**(2), p 127-136
25. J.A. Pattison, S. Celotto, A. Khan, and W. O'Neill, Standoff Distance and Bow Shock Phenomena in the Cold Spray Process, *Surf. Coat. Technol.*, 2008, **202**(8), p 1443-1454
26. S.H. Zahir, W. Yang, and M. Jahedi, Characterization of Cold Spray Titanium Supersonic Jet, *J. Therm. Spray Technol.*, 2008, **18**(1), p 110-117
27. O. Stier, Fundamental Cost Analysis of Cold Spray, *J. Therm. Spray Technol.*, 2014, **23**(1-2), p 131-139
28. H. Katanoda, M. Fukuhara, and N. Iino, Numerical Study of Combination Parameters for Particle Impact Velocity and Temperature in Cold Spray, *J. Therm. Spray Technol.*, 2007, **16**(5-6), p 627-633
29. M. Stanislas, K. Okamoto, C.J. Kähler, and J. Westerweel, Main Results of the Second International PIV Challenge, *Exp. Fluids*, 2005, **39**(2), p 170-191
30. R.C. Dykhuizen and M.F. Smith, Gas Dynamic Principles of Cold Spray, *J. Therm. Spray Technol.*, 1998, **7**(2), p 205-212
31. S. Yin, M. Meyer, W.-Y. Li, H. Liao, and R. Lupoi, Gas Flow, Particle Acceleration, and Heat Transfer in Cold Spray: A review, *J. Therm. Spray Technol.*, 2016